Title

The mechanism and kinetics of methyl isobutyl ketone synthesis from acetone over ion-exchanged hydroxyapatite

Authors

Ho, Christopher R
Zheng, Steven
Shylesh, Sankaranarayanapillai
et al.

Publication Date

2018-09-01

DOI

10.1016/j.jcat.2018.07.005

Peer reviewed

Journal of Catalysis 365 (2018) 174–183

Contents lists available at ScienceDirect

Journal of Catalysis

journal homepage: www.elsevier.com/locate/jcat

The mechanism and kinetics of methyl isobutyl ketone synthesis from acetone over ion-exchanged hydroxyapatite

Christopher R. Ho [a,b], Steven Zheng [a], Sankaranarayanapillai Shylesh [a,b], Alexis T. Bell [a,b,*]

[a] Department of Chemical and Biomolecular Engineering, University of California, Berkeley, CA 94720-1462, United States
[b] Chemical Sciences Division, Lawrence Berkeley National Laboratory, Berkeley, CA 94720, United States

ARTICLE INFO

Article history:
Received 9 May 2018
Revised 26 June 2018
Accepted 2 July 2018
Available online 18 July 2018

Keywords:
Aldol condensation
Acid-base strength
C—C coupling
Green chemistry

ABSTRACT

The synthesis of methyl isobutyl ketone (MIBK) can be carried out by the condensation of acetone in the presence of hydrogen over a supported metal catalyst. Previous studies have shown that hydroxyapatite is an excellent catalyst for condensation reactions. The present investigation was undertaken in order to elucidate the reaction mechanism and site requirements for acetone coupling to MIBK over a physical mixture of hydroxyapatite and Pd/SiO_2. The reaction is found to proceed by consecutive aldol addition to form diacetone alcohol (DAA), dehydration of DAA to mesityl oxide (MO), and hydrogenation of MO to MIBK. The products formed by feeding DAA and MO reveal that aldol addition of acetone is rapid and reversible, and that the subsequent dehydration of DAA is rate-limiting. Pyridine and CO_2 titration show that aldol dehydration occurs over basic sites via an E_{1cB} mechanism. A series of cation-substituted hydroxyapatite samples were prepared by ion-exchange to further investigate the role of acid-base strength on catalyst performance. Characterization of these samples by PXRD, BET, ICP-OES, XPS, CO_2-TPD, and Raman spectroscopy demonstrated that the exchange procedure used does not affect the bulk properties of hydroxyapatite. DFT calculations reveal that in addition to affecting the Lewis acidity/basicity of the support, the size of the cation plays a significant role in the chemistry: cations that are too large (Ba^{2+}) or too small (Mg^{2+}) adversely affect reaction rates due to excessive stabilization of intermediate species. Strontium-exchanged hydroxyapatite was found to be the most active catalyst because it promoted α-hydrogen abstraction and C—O bond cleavage of DAA efficiently.

1. Introduction

Acetone is produced industrially as a byproduct in the production of cumene. While acetone can be used as a solvent, its value can be increased by upgrading it to form methyl isobutyl ketone (MIBK) [1,2]. MIBK is used for manufacturing paints, rubbers, and pharmaceuticals [3]. It is also used for liquid-liquid extraction of precious metals, due to its low miscibility with water [1]. Traditionally, MIBK is produced in a batch reactor in three steps: acetone coupling to form diacetone alcohol catalyzed by sodium hydroxide, diacetone alcohol dehydration to mesityl oxide catalyzed by sulfuric acid, and mesityl oxide hydrogenation to MIBK over a metal catalyst (Scheme 1) [1]. More recently, it has been demonstrated that MIBK can be produced more efficiently via a single step using a metal-supported catalyst [4–11]. The support catalyzes acetone condensation to mesityl oxide and the metal promotes the subsequent hydrogenation of this intermediate to MIBK. The acidity/basicity of the support dictates whether acetone condensation follows an enol or enolate mechanism, and the strength of the acid/base sites affects the rate of reaction [4]. While many different supports (ionic resins [5,6], metal oxides [7–9], mixed metal oxides [10,11]) are known to be active for MIBK formation, the relationship between support acid/base strength and catalytic performance remains unclear because it is difficult to modify the chemical properties of the support without changing its structure. For example, several groups have studied aldol condensation over MgO/Al_2O_3 with varying Mg/Al ratios [12,13]. Areal reaction rates are highest over pure MgO, which has been attributed to the high density of strongly basic O^{2-} sites that enhance α-hydrogen abstraction [12]. However, changing the Mg/Al ratio also affects the bulk structure and crystallite size of the supported MgO, making it difficult to determine whether differences in rates are attributed solely to differences in acid/base properties.

Hydroxyapatite (HAP; $Ca_5(PO_4)_3OH$) is an attractive candidate support because it can accommodate a host of cationic ($Ca^{2+} \rightarrow Mg^{2+}$, Sr^{2+}, Ba^{2+}, Co^{2+}, Ni^{2+}, Cu^{2+}, Zn^{2+}, Pb^{2+}, Cd^{2+}) [14–17] and anionic ($PO_4^{3-} \rightarrow VO_4^{3-}$, AsO_4^{3-}, CO_3^{2-}, SO_3^{2-}; $OH^- \rightarrow F^-$, Cl^-)

* Corresponding author at: Department of Chemical and Biomolecular Engineering, University of California, Berkeley, CA 94720-1462, United States.
E-mail address: bell@cchem.berkeley.edu (A.T. Bell).

https://doi.org/10.1016/j.jcat.2018.07.005
0021-9517/

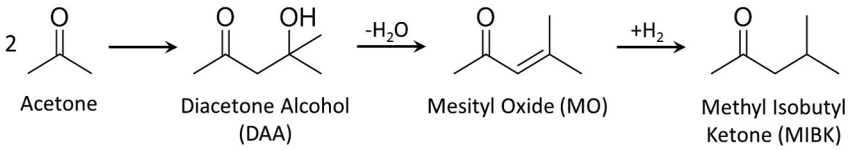

Scheme 1. Acetone condensation to methyl isobutyl ketone (MIBK).

[18–20] substitutions that can affect its catalytic performance. The unsubstituted form of HAP has been shown to be effective for a number of C—C bond forming processes, including Guerbet coupling of ethanol and dimerization of 2-hexanone [21,22]. However, there have been relatively few studies showing the effects of ion substitution on catalyst activity and selectivity. Ogo et al. have shown that HAP substituted with VO_4^{3-} anions increases its selectivity for acetaldehyde dimerization to crotonaldehyde [23]. Silvester et al. have prepared CO_3^{2-} and Sr^{2+} substituted samples of HAP and found that a balance of acid and base sites is needed to maximize selectivity for the Guerbet coupling of ethanol [24,25]. It should be noted, though, that each of these catalysts was prepared by incorporating the new cations or anions during synthesis via co-precipitation. While this approach does not affect the crystal structure of HAP, it can induce changes in particle morphology and acid/base site densities, as shown by electron microscopy and TPD desorption experiments, respectively [18,26].

An alternative approach for introducing new cations and anions is post-synthetic ion-exchange, a method that enables modification of the surface composition without alteration of the bulk properties [16]. Several authors have reported the successful substitution of Ca^{2+} by other divalent cations using this approach [27,28]. However, the exchange process can lead to partial dissolution and surface restructuring of HAP under certain conditions, which should be avoided in order to make a fair comparison between catalysts [29]. Prior studies have shown that the dissolution process can be minimized by performing the exchange in neutral to basic solutions to limit HAP solubility [30].

The goal of this study was to investigate the mechanism and kinetics of MIBK synthesis over HAP and to identify the role of cations other than Ca^{2+} at the catalyst surface on the catalyst activity. To this end, we describe a method for preparing a set of cation-exchanged HAP samples (Mg, Ca, Sr, Ba, Cd, Pb) and show through various characterization techniques that the bulk structure is unaffected. The acid/base properties are modulated through the identity of the cation, which in turn affects the catalyst performance. The mechanism is found to initiate with the condensation of acetone to diacetone alcohol, which then undergoes dehydration to form mesityl oxide. This rate-limiting step is catalyzed by basic sites on the surface of HAP. Since the reaction of acetone to mesityl oxide is endoergic, mesityl oxide needs to be hydrogenated to MIBK using silica-supported Pd in order to achieve high conversions of acetone. The rate of acetone condensation to mesityl oxide is strongly dependent on the basicity of O on the catalyst surface, which is influenced by the nature of the divalent cation connected to the O atom. Highest activity is observed when Ca^{2+} is replaced by Sr^{2+}. Density functional theory (DFT) calculations were performed to map out the free energy landscape for the condensation of acetone to mesityl oxide and to identify how the properties of the divalent cation connected to lattice O atoms affect their activity for the dehydration of diacetone alcohol.

2. Experimental methods

2.1. Catalyst synthesis

Hydroxyapatite (HAP) was synthesized using a modification of the procedure reported by Tsuchida et al. [31] and Hanspal et al. [32] Aqueous solutions of 0.25 M $Ca(NO_3)_2{\cdot}4H_2O$ and 0.55 M $(NH_4)_2HPO_4$ were prepared and brought to a pH of 11 by addition of ammonium hydroxide. The calcium solution was added dropwise to the phosphorus solution at room temperature and stirred for 0.5 h before heating to 353 K for an additional 3 h. The resulting slurry was filtered and washed with DI water.

The calcium in HAP was exchanged with other cations by ion-exchange. Mg-, Sr-, Ba-, Cd- and Pb-HAP were prepared by adding 0.2 g of HAP into a 30 mL aqueous solution of the respective nitrate precursor ($Mg(NO_3)_2{\cdot}6H_2O$, $Sr(NO_3)_2$, $Ba(NO_3)_2$ = 2.5 mmol; $Cd(NO_3)_2{\cdot}4H_2O$, $Pb(NO_3)_2$ = 0.25 mmol). Smaller quantities of Cd and Pb nitrates were used to offset the greater ease of substitution of these cations compared to Mg, Sr, and Ba [33,34]. The pH of the HAP solution was adjusted to 7 by addition of HNO_3 or NH_4OH. For Pb substitution, a solution pH of 6 was used to avoid precipitation of lead hydroxides. The solution was stirred for 5 h at 298 K, filtered, washed with DI water, and dried at 393 K overnight in air.

3 wt%Pd/SiO_2 was prepared by incipient wetness impregnation using an aqueous solution of $Pd(NO_3)_2{\cdot}2H_2O$ on a silica support (SiliaFlash150A). The catalyst was dried at 298 K overnight and calcined in 100 mL/min of air at 823 K for 2 h before use.

2.2. Characterization techniques

Powder X-ray diffraction (PXRD) patterns were taken with a Bruker D8 GADDS diffractometer equipped with a Cu-Kα source (40 kV, 40 mA). BET surface areas were calculated from nitrogen adsorption isotherms obtained using a Micromeritics Gemini VII 2390 surface area analyzer after degassing the catalyst overnight at 393 K. Basic site density was measured by temperature-programmed desorption (TPD) of CO_2 using a Micromeritics AutoChem II 2920 instrument equipped with a thermal conductivity detector. Samples were pretreated under He flow at 823 K for 1 h before cooling to 313 K. CO_2 (30 mL min^{-1}) was introduced for 0.5 h at 313 K, after which the samples were purged with He for 0.5 h at 313 K to remove any physisorbed species from the surface. Desorption of adsorbed CO_2 was performed in flowing He (50 mL min^{-1}) using a temperature ramp rate of 5 K min^{-1}.

Bulk compositions were determined by ICP-OES using an Optima 7000 DV instrument with yttrium as an internal standard. Surface compositions were determined using a Kratos Axis Ultra DLD X-ray photoelectron spectrometer (XPS). Measurements were performed with an Al-Kα source (15 kV, 10 mA) at a pressure of ~9 nTorr. Kinetic energies were defined by shifting the spectra so that the C 1s binding energy of adventitious carbon was 284.8 eV. Initial elemental compositions were obtained by normalizing the intensity of the characteristic peaks with an internally calibrated relative sensitivity factor. However, this normalization relies on the assumption that the sample is homogeneous across the probing depth of photoelectrons (~1 nm), which was found to be invalid when compared to elemental analysis data. Instead, the degree of ion-exchange on the surface was calculated by using the general XPS equation:

$$I_{element} = F_x S\sigma \int_0^{0.3nm} c_{element} e^{-z/\lambda_{Ek}\cos\theta} dz \quad (1)$$

$I_{element}$ = intensity of XPS peak
F_x = x-ray flux

S = transmission function
σ = cross-section for photoemission
n_{Ek} = normalizing factor (transmission function, photoelectron cross section)
$c_{element}$ = concentration
λ_{EK} = mean free path of photoelectron

Photoelectron cross-sections were determined using Scofield factors [35]. The inelastic mean free path was determined theoretically from the TPP-2M formula using the Quases program [36]. The structural input of HAP was approximated with tricalcium phosphate because of its similarities in composition and bandgap [37,38]. The concentration of Ca in the sample was determined with either the Ca 2s or Ca 2p photoemission, depending on the overlap in binding energies of the exchanged cation. The concentration of P was determined in a similar manner (using P 2s or P 2p emission) The substituted cations were quantified using the Ba 3d, Cd 3d, Mg KLL, Pb 4p and Sr 3p/2 core levels. Fitting of Eq. (1) to experimental data was performed using the XPS Multiquant software [39].

2.3. Measurements of catalytic activity

Measurements of reaction rates were carried out using a quartz-tube, packed-bed reactor (10 mm inner diameter). Quartz wool was placed below the catalyst bed to hold the catalyst in place. The reactor temperature was maintained using a tube furnace equipped with a Watlow temperature controller and a K-type thermocouple. Prior to reaction, the catalyst was treated in 30 cm^3 min^{-1} of H_2 at 823 K for 1 h before cooling to the reaction temperature.

In a typical experiment, acetone was introduced into a He stream flowing at 30 cm^3 min^{-1} using a syringe pump (Cole Parmer, 74,900 series). Diacetone alcohol, mesityl oxide, water, and pyridine were also fed in a similar manner. All experiments were carried out at a pressure of 1 atm. Product streams were analyzed by gas chromatography using an Agilent 6890A GC fitted with a HP-5 capillary column (30 m × 0.32 mm × 0.25 μm) and a flame ionization detector. Kinetic measurements of acetone condensation were carried out at <5% conversion, where the selectivity of MIBK was always >95%. Diisobutyl ketone was the only other product observed in significant amounts. The reported condensation rates were calculated by assuming that diisobutyl ketone is formed by condensation of acetone and MIBK. One additional experiment was performed at an acetone conversion of 27.8% (Table S1). Under these conditions, the measured carbon balance was 95 ± 5%. 2-propanol and methyl isobutyl carbinol were observed as additional products. These products are presumably formed by the hydrogenation of acetone and MIBK, respectively.

Supplementary data associated with this article can be found, in the online version, at https://doi.org/10.1016/j.jcat.2018.07.005.

2.4. Theoretical calculations

Periodic density functional theory (DFT) calculations were performed with the Vienna Ab Initio Simulation Package (VASP) using the projector augmented wave method (PAW) [40]. The PBE generalized-gradient-approximation (GGA) exchange-correlation functional was used with a kinetic cutoff energy of 400 eV [41]. Brillouin-zone integrations were performed using the gamma point [42]. Optimization was done with the conjugate-gradient algorithm until the total atomic forces were below 0.01 eV $Å^{-1}$. Refinements in the size of the k-point mesh and cutoff energy showed that the energies were converged with a maximum error of ±0.03 eV. The DFT-D3 method with Becke-Jonson damping was used to correct for dispersion [43]. Transition state searches were done using the climbing nudged elastic band and dimer methods [44,45]. Frequency calculations were run at P = 1 atm and T = 373 K. Enthalpies and entropies were determined using the quasi-rigid rotor-harmonic oscillator approximation [46,47].

The hexagonal structure of HAP with $P6_3$ symmetry was used to construct a 1 × 2 × 2 supercell [48]. Acetone adsorption and enolate formation on HAP were studied on the hydroxyl-rich termination of the (0 1 0) plane since it has been proposed that this plane is active for C—C coupling reactions [21,49]. A 20 Å vacuum gap above the surface was used to minimize unwanted interactions between adjacent surfaces. The lattice parameters were optimized using the bare surface of each structure and subsequently fixed for the ensuing calculations. Atoms in the bulk were also fixed after optimization, while the top two layers were allowed to relax in the calculations. The ion-exchanged HAP catalyst were modeled by substituting one of the four equivalent Ca atoms on the surface of the (0 1 0) plane with a divalent metal.

Several gas phase calculations with deuterated and hydrogenated molecules were also carried out using the Q-Chem simulation package [50]. Calculations were performed at the ωB97X-D/6-311++G(3df,3pd) level of theory.

3. Results and discussion

3.1. Characterization of IE-HAP catalysts

The structural properties of as-prepared catalysts are shown in Table 1. The surface areas for all samples are between 87 and 92 m^2/g with the exception of Pb-HAP, which is 71 m^2/g. The difference in mass between Ca and the heavier Pb atom does not fully account for the difference in surface area (Table 1), suggesting that the surface of HAP is modified by a dissolution/reprecipitation mechanism during the exchange procedure with Pb^{2+}. Indeed, TEM images taken by Yasukawa et al. have shown that incorporation of Pb via ion exchange induces a change in morphology and increase the aspect ratio of HAP [27]. All major diffraction peaks observed in the powder XRD patterns can be ascribed to a nanocrystalline apatite structure (Fig. 1) [49,51]. There is no shift in the 2θ peak positions for any sample, indicating that the lattice parameters for the bulk structure do not expand or contract due to incorporation of metal cations. No additional metal oxide phases can be seen by XRD, although this does not exclude the possible presence of very small metal oxide nanoparticles. The particle size of the cation-exchanged apatite as determined by the Scherrer

Table 1
Properties of ion-exchanged HAP catalysts.

Catalyst	Surface area		Bulk (Ca + M)/P ratio	Bulk Ca/M ratio	Depth of exchange layer (nm)	Basic site density (μmol CO_2/m^2)
	m^2/g	m^2/mol HAP ($Ca_{10-x}M_x(PO_4)_6(OH)_2$)				
Ca-HAP	87	8.7×10^4	1.69	–	–	0.45
Mg-HAP	92	9.2×10^4	1.74	0.024	0.8 ± 0.3	0.39
Sr-HAP	87	8.8×10^4	1.67	0.033	1.1 ± 0.4	0.46
Ba-HAP	88	8.9×10^4	1.76	0.018	1.0 ± 0.7	0.45
Pb-HAP	71	7.2×10^4	1.74	0.084	0.6 ± 0.4	0.41
Cd-HAP	92	9.3×10^4	1.71	0.076	0.5 ± 0.4	0.40

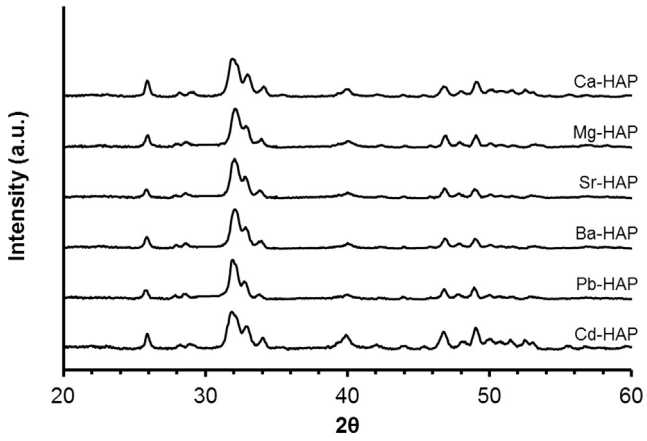

Fig. 1. PXRD patterns of ion-exchanged HAP catalysts.

equation using the (0 0 2) and (3 0 0) diffraction peaks are 22 and 17 nm, respectively, for all samples, indicating that there is a slight elongation along the c-axis. This observation is consistent with literature reports that HAP tends to grow along the c-axis during wet synthesis [49]. TEM images of HAP before and after exchange with Sr^{2+} reveal similar morphologies, with a distribution of semi-spherical particles ranging from 10 to 40 nm in diameter with an average size of 20 nm (Figs. S1 and S2). Comparison of the images shows that the ion-exchange procedure does not affect particle size or shape.

Raman spectroscopy was used to confirm the absence of metal oxide nanoparticles (Fig. 2). Four sets of vibrational frequencies are found at 400–485 cm^{-1}(ν_2), 550–630 cm^{-1}(ν_4), 910–1000 cm^{-1} (ν_1), and 1020–1085 cm^{-1}(ν_3) which correspond to the stretching and bending modes of phosphate groups [52]. No bands corresponding to other calcium phosphate phases such as β-TCP and orthophosphate are detected [53]. An additional band is observed at 930 cm^{-1} for the Pb-HAP sample which is ascribed to phosphate groups that are adjacent to lead atoms [54]. Lead forms a stronger covalent bond with the nearby oxygen and causes a shift in the phosphate stretching mode [54]. This shift is not observed in the other substituted HAP samples, most likely because the other metals were exchanged at lower loadings and are more ionic in character, leading to more overlap with the main ν_1 stretching mode at 960 cm^{-1}.

Elemental analysis (ICP-OES) shows that the degree of exchange in HAP samples is dependent on the exchanged metal and decreases in the order of Pb^{2+} > Cd^{2+} > Sr^{2+} > Mg^{2+} > Ba^{2+}, in good agreement with the literature [33,34]. The Pb and Cd samples were synthesized using a lower concentration of metal nitrate solution compared to the alkali earth samples (7.5 mM vs 75 mM), but still had a greater level of exchanged metal. This finding is consistent with DFT results from Murata showing that Pb and Cd have lower ionic substitutional energies compared to other elements [55].

XPS was used to determine the location of the exchanged metal species. ICP-OES provides information about bulk composition while XPS is surface sensitive. By comparing the results of both techniques, it is possible to determine the degree of ion-exchange at the catalyst surface. It is helpful to consider the two extremes regarding the location of the exchanged metal species. In the first extreme, we assume the IE-HAP synthesis procedure produces a homogeneous distribution of the exchanged cation with no difference in the bulk and surface elemental compositions. However, this assumption leads to a contradiction in predicted compositions as measured by ICP-OES and XPS (Fig. S3). In the other extreme, we assume that ion-exchange happens at the surface of HAP with limited dissolution/re-precipitation. This scenario would result in the substituted cation residing only in the top monolayer of HAP. Using this assumption, the calculated surface compositions from ICP-OES and XPS data give similar results (Fig. 3), indicating that the exchanged cations are present predominantly at the surface.

A more detailed analysis of the distribution of the exchanged cations was performed by modeling the ion-exchanged HAP as a 20 nm spherical particle composed of two layers: an outer surface layer containing a homogeneous mixture of Ca^{2+} and the exchanged cation and an inner core that only contains the native Ca^{2+} cations. The ICP-OES and XPS data could be fit to this model in order to obtain an estimate for the thickness of the outer exchange layer. As shown in Table 1, the depth of the exchange layer for all samples is between 0.5 and 1.1 nm. Since the average thickness of one monolayer in HAP is ~0.3 nm, the exchanged cations appear to be able to penetrate down to a maximum of two to three monolayers from the surface.

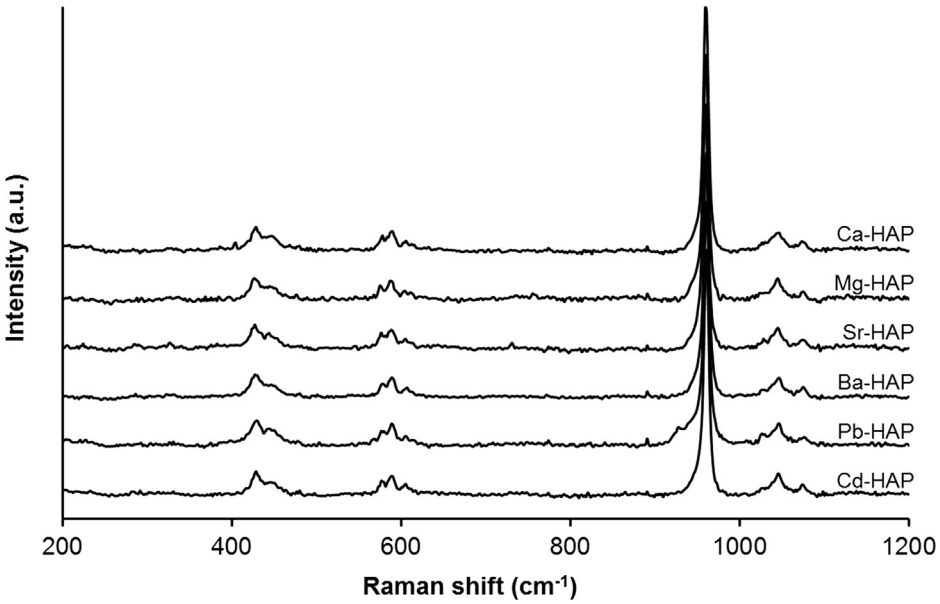

Fig. 2. Raman spectra of ion-exchanged HAP catalysts.

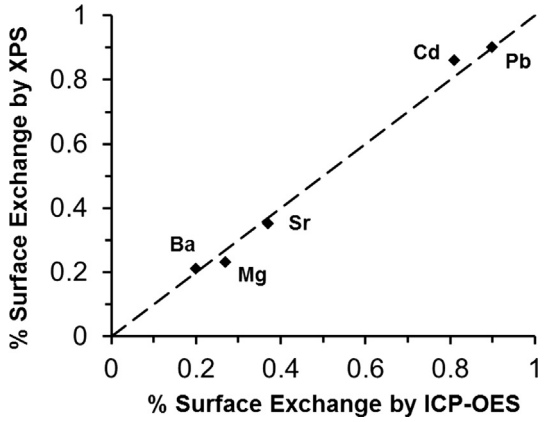

Fig. 3. Calculated fraction of exchanged cations using elemental composition data acquired by ICP-OES or XPS assuming the exchange only occurs at the surface monolayer of HAP. The dotted line represents perfect agreement between ICP-OES and XPS measurements.

Temperature-programmed desorption (TPD) of CO_2 was performed to determine the number of basic sites over the IE-HAP samples. As shown in Table 1, all samples have similar basic site density, which is further proof that no major surface restructuring occurs during ion-exchange treatment. Mg-, Ca-, Sr-, Ba- and Cd-HAP exhibit two CO_2 desorption peaks at 348 and 623 K which correspond to weak and medium strength basic sites, respectively, whereas Pb-HAP exhibits only one broad peak from 348 K to 573 K (Fig. S4) [56].

3.2. Acetone condensation over IE-HAP

Scheme 1 shows how we envision the condensation of acetone to produce MIBK proceeds. The first step is the reversible condensation of acetone to DAA, which then undergoes dehydration to form mesityl oxide (MO). This overall reaction is thermodynamically unfavorable and is characterized by an equilibrium conversion of 4.7% at 373 K, which we observed experimentally. This corresponds to ΔG_{rxn} = +6.9 kcal/mol, in good agreement with the value obtained from DFT calculations, ΔG_{rxn} = +7.7 kcal/mol. To overcome this thermodynamic limitation, MO must be hydrogenated to MIBK over 3 wt% Pd/SiO_2. This shifts the equilibrium towards the right and simplifies measurement of the reaction kinetics for formation of MIBK. At low partial pressures of acetone (< 0.5 kPa) and slightly higher reaction temperatures (423 K), the rate of MIBK formation is 1.5 order with respect to acetone (Fig. S5), suggesting that the rate-limiting step occurs during the coupling of two acetone-derived surface species or involves a reaction with an intermediate formed from the bimolecular coupling of two acetone molecules.

To support the reaction mechanism presented in Scheme 1, various intermediates were fed over HAP to determine the relative rates of each reaction step (Table 2). When DAA is used as the reactant, quantitative conversion is reached with 97% selectivity to acetone. Even after H_2 is added to increase the rate of hydrogenation, DAA is converted to acetone with 87% yield, indicating that the retroaldol reaction is much faster than the rate of DAA dehydration. This suggests that acetone and DAA are in pseudo-equilibrium. A mixture of MO, H_2O and H_2 was fed over HAP to compare the relative rates of dehydration and hydrogenation. MIBK was formed with 99% yield, indicating that hydrogenation is rapid in the presence of H_2 and dehydration of DAA is the slowest step. Identical studies over Cd-, Mg-, Sr- and Ba-HAP gave similar conversions and product selectivities (Table S2), showing that the mechanism is similar over all ion-exchanged catalysts.

Mechanistic studies of aldehyde dimerization over HAP at 533–673 K by Young et al. and Hernández-Giménez et al. have suggested that product desorption is slow in the absence of a hydrogen donor [57,58]. If product desorption is rate-limiting, then every surface reaction prior to that step is quasi-equilibrated, including the dehydration of DAA. To determine whether this idea is applicable to acetone dimerization at 373–423 K, it is important to note that dehydration of DAA produces H_2O. Thus, if surface dehydration is quasi-equilibrated, the addition of H_2O will decrease the concentration of adsorbed MO species, and the reaction rates should be inverse order with respect to H_2O partial pressure under all operating conditions (Scheme S1). Experimentally, the rate of MIBK formation is −0.1 order with respect to H_2O at high acetone partial pressures (20 kPa), suggesting that product desorption is not rate-limiting (Fig. S6). Instead, H_2O appears to inhibit the rate of reaction by competitive adsorption.

Kinetic isotope experiments were conducted using H_6-acetone/H_2 and D_6-acetone/D_2 in order to verify the conclusions drawn from the co-feed studies. If k_H/k_D is significantly greater than one, the rate-limiting step involves the cleavage of a bond involving a hydrogen atom. However, if reaction rates are invariant with deuteration, this would infer that the cleavage of a C—C or C—O bond is rate-limiting. Experimentally, an inverse isotope effect of k_H/k_D = 0.55 is observed. To understand the origin of this result, gas-phase DFT calculations were performed with deuterated and non-deuterated molecules (Table 3). H_6-acetone dimerization to DAA is energetically uphill (ΔG_{rxn} = +10.1 kcal/mol) and the subsequent dehydration to MO is only mildly favorable (ΔG_{rxn} = −2.3 kcal/mol), which

Table 2
Conversion and yield of key reaction intermediates over HAP. T = 373 K; $mass_{HAP}$ = 0.01 g; $mass_{Pd/SiO2}$ = 0.04 g ; $P_{DAA\ or\ MO,H2O}$ = 0.1 kPa; P_{H2} = 0 or 5 kPa; total gas flow rate at STP = 100 $cm^3\ min^{-1}$.

Reactant	Conversion (%)	Yield (%)			
		Acetone	DAA	MO	MIBK
DAA	>99	97	–	3	0
DAA + H_2	>99	87	–	0	13
MO + H_2O + H_2	>99	1	0	–	99

Table 3
DFT calculations of reaction free energies using hydrogenated and deuterated reactants.

Reaction	Non-deuterated		Deuterated	
	ΔH_{rxn} (kcal/mol)	ΔG_{rxn} (kcal/mol)	ΔH_{rxn} (kcal/mol)	ΔG_{rxn} (kcal/mol)
2 Acetone → DAA	−7.69	10.06	−8.32	9.66
2 Acetone → MO + H_2O	6.55	7.72	6.43	7.62
2 Acetone + H_2 → MIBK + H_2O	−22.33	−8.98	−26.06	−13.81

supports the conclusion that acetone and DAA are in pseudo-equilibrium. In contrast to dimerization of H_6-acetone, dimerization of D_6-acetone (ΔG_{rxn} = +9.7 kcal/mol) is more facile thermodynamically. This is due to a change in hybridization geometry from sp^2 (acetone – carbonyl) to sp^3 (DAA – hydroxyl) [59]. The out-of-plane bending mode is stronger for sp^3 geometry, which leads to a larger reduction in zero point energy upon H → D substitution. For a given H_6-/D_6-acetone partial pressure, the calculated gas-phase equilibrium concentration of D_{12}-DAA is 1.3x times greater than the concentration of H_{12}-DAA. This translates to a predicted equilibrium isotope effect of $k_H/k_D \approx 0.67$, which agrees qualitatively with the experimental observation. Therefore, the observed inverse isotope effect is attributed to a change in the equilibrium constant between acetone and DAA. Similar isotope effects have been observed for other carbonyl addition reactions [60,61].

Several related studies of aldol condensation reactions over HAP and other metal oxides report that dehydration of the aldol intermediate is facile [21,61,62]. However, these studies were conducted at higher temperatures (>533 K) compared to the current work (373 K). Monomolecular dehydration is favored entropically due to the formation of two products from one reactant. Thus, dehydration of the addition product becomes more difficult at lower temperatures relative to other steps such as enolate formation and C—C coupling. This is likely why many liquid phase studies of acetone condensation (which are typically conducted at T < 373 K) report that aldol dehydration is slow compared to the formation of the addition product [63,64].

In-situ titration experiments were performed to determine the site requirements for acetone condensation (Fig. 4). Co-feeding pyridine (1 kPa) does not significantly affect MIBK formation rates, which indicates that acid sites are weak and cannot bind pyridine strongly, consistent with DRIFTS studies of adsorbed pyridine reported by Hill et al. [65] By contrast, introducing CO_2 decreases rates by more than an order of magnitude, suggesting that the rate-limiting dehydration of DAA mainly occurs over basic sites. At first glance, this may seem contradictory to findings by Kibby et al., who found that alcohol dehydration over HAP requires acid sites [66]. However, those reactions were performed with unactivated alcohols at much higher temperatures (500–600 K). The dehydration of DAA is more facile than typical alkanols because the C_α—H bond is weakened by the nearby carbonyl group, which makes the α-hydrogen more prone to attack by a base. The ease of α-hydrogen abstraction suggests that DAA dehydration can proceed via an E_{1cB} mechanism at low temperatures in which an enolate species is formed via α-hydrogen abstraction by a basic surface oxygen atom. The hydroxyl group in DAA is subsequently eliminated to form MO and water. E_{1cB} mechanisms are observed commonly in homogeneous aldol dehydration reactions with NaOH and have been proposed for alcohol dehydration over solid base catalysts such as MgO [67–69]. A central question in the E_{1cB} mechanism is whether proton abstraction or subsequent carbanion decomposition is rate-limiting. This issue can be addressed by noting that that proton abstraction of DAA and acetone both occur at the α-carbon next to the carbonyl group. Since enolate formation of acetone is rapid and reversible over HAP, it suggests that proton abstraction of DAA is rapid as well. This conclusion is in agreement with the observed inverse isotope effect, indicating that C-H bond cleavage is not rate-limiting. Thus, DAA and its enolate are in pseudo-equilibrium and the subsequent elimination of OH^- to form MIBK is slow and irreversible.

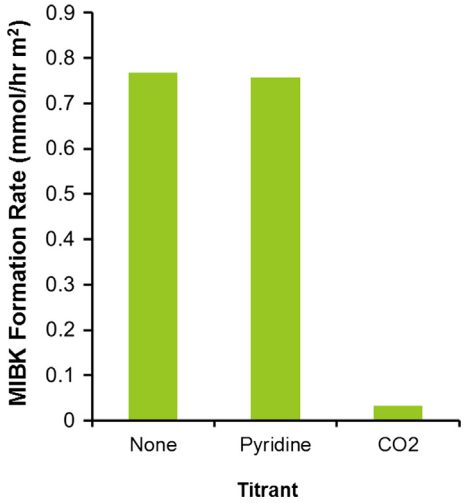

Fig. 4. Effect of titrant on MIBK formation rate. Reaction conditions: $P_{Acetone}$ = 5 kPa, P_{H2} = 5 kPa, $P_{Titrant}$ = 1 kPa, T = 373 K, $mass_{HAP}$ = 0.01 g, $mass_{Pd/SiO2}$ = 0.04 g.

The results reported to this point show that the surface oxygen atoms of HAP are responsible for proton abstraction from DAA. Therefore, we hypothesized that increasing the basic strength of these oxygen atoms should enhance the overall reaction rate. This was tested by measuring acetone condensation rates over the various ion-exchanged HAP catalysts. Since these catalysts contain both Ca^{2+} sites and M^{2+} sites, the extent of exchange needs to be considered to determine the true effect of the exchanged cation on reaction rates. Calculations show that the bonding between Ca—O in HAP is mostly ionic with localized electron density [55]. Substitution of Ca^{2+} with another divalent cation affects the partial charge of the adjacent oxygen atoms, but does not significantly influence the electronics of oxygen atoms in the second shell because of the ionic nature of the bonds. If the electron density away from the substituted site is invariant with the substitution, then the apparent reaction rates measured over the ion-exchanged samples can be decoupled linearly into the sum of two contributions: rates over the native Ca^{2+} sites and rates over the exchanged M^{2+} sites. The rates over the native Ca^{2+} sites are measured over the original Ca-HAP sample. For the ion-exchanged samples, the rates over the exchanged M^{2+} sites can be extracted by knowing the fractional surface coverage of Ca^{2+} and M^{2+}. The assumption of local electron density does not hold when substituting Ca^{2+} with Pb^{2+} because of the strong covalent Pb—O bonds [70]. The apparent MIBK formation rate over Pb-HAP is over 140 times slower than Ca-HAP even though only 90% of the Ca sites are replaced with Pb, showing that activity of Ca sites decreases with substitution of Ca^{2+} by Pb^{2+}.

MIBK formation rates of each sample were normalized by the surface area or basic site density (as determined by CO_2-TPD) after accounting for the extent of exchange and are plotted in Fig. 5. Since the electron density of the oxygen atoms are influenced by the neighboring cations, the electronegativity of the cation, which is a measure of the propensity to attract electrons, can be used as a descriptor of basicity. As the basicity of the catalyst increases from Pb^{2+} to Sr^{2+}, the reaction rates also increase. However, even though Ba-HAP is more basic than Sr-HAP, it is three times less active, suggesting that either an appropriate balance of acid and base strength is necessary, or a more detailed descriptor is needed. The measured activation energies are in relative agreement with the rates. With increasing basicity, the apparent activation energy decreases from 16 kcal/mol for Cd-HAP to 11 kcal/mol for Sr-HAP and then increases to 14 kcal/mol for Ba-HAP.

DFT calculations were performed to gain more insight into the mechanism of DAA dehydration. The OH-terminated (0 1 0) plane on HAP was chosen as the model surface because it is preferentially exposed under the used synthesis conditions (co-precipitation method, high pH) [49]. Furthermore, studies by Tsuchida et al. [31] and Rodrigues et al. [71] have shown that HAP catalysts with

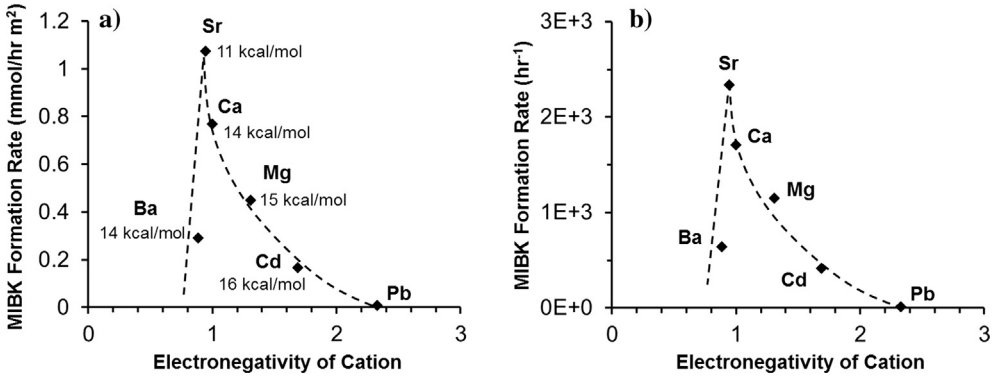

Fig. 5. Effect of cation substitution on MIBK formation rate normalized by (a) surface area and (b) number of basic sites. The dotted line is meant to guide the eye. Reaction conditions: $P_{Acetone}$ = 15 kPa, P_{H2} = 5 kPa, T = 373 K, $mass_{HAP}$ = 0.01 g, $mass_{Pd/SiO2}$ = 0.04 g.

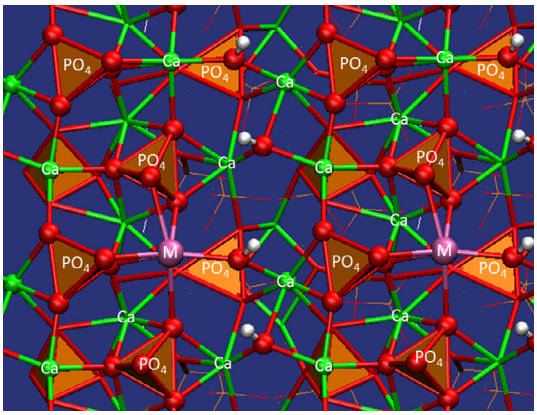

Fig. 6. Model of OH-terminated (0 1 0) plane on HAP. Green is calcium, red is oxygen, and white is hydrogen. Orange tetrahedrons represent phosphate groups.

higher Ca/P ratios exhibit higher rates for aldol condensation, suggesting that the active site is located on the OH-terminated (0 1 0) plane, which possesses the highest Ca/P ratio of all low index planes. DFT studies by Corno et al. demonstrate that the stoichiometric (0 1 0) surface will spontaneously undergo hydroxylation in the presence of water (a byproduct in the aldol dehydration step) to form a surface that resembles the OH-terminated (0 1 0) plane [72,73]. The surface Ca atoms on the OH-terminated (0 1 0) plane are located in the Ca(II) sites adjacent to the columnar hydroxyl groups, as shown in Fig. 6. However, a pristinely cut, OH-terminated (0 1 0) surface on HAP is typically not observed experimentally. Instead, some of the surface phosphate groups hydrolyze to form weakly acidic POH groups, as evidenced by IR spectroscopy [74]. In addition, the Ca/P ratio on the surface as measured by XPS is usually lower than that of the bulk, suggesting that a fraction of the surface cation sites contains a pair of protons or a proton plus hydroxyl group vacancy in place of Ca^{2+} [75,76]. Although these various modifications may play a role in condensation reactions, the structures and geometries of these surfaces have not been clearly defined. Thus, modeling and structure calculations of these hypothetical surfaces are beyond the scope of the current work.

We first considered the adsorption of DAA onto HAP. Two adsorption geometries were considered: a monodentate adsorption mode for which only the carbonyl oxygen is bound to a Ca^{2+} ion and a bidentate adsorption mode for which both the carbonyl and hydroxyl groups are bound to the same Ca^{2+}. We found that the monodentate adsorption was thermodynamically uphill (ΔG_{ads} = +14.2 kcal/mol) due to the entropy loss upon adsorption, whereas the bidentate adsorption was found to be favorable (ΔG_{ads} = −5.1 kcal/mol). The energetic stabilization comes from the additional Ca-O interaction as well as the H-bonding between the DAA hydroxyl group and an adjacent phosphate group, shown in Scheme 2.

Fig. 7 illustrates the computed Gibbs free energy profile for the reaction of adsorbed DAA on the surface of Ca-HAP. After

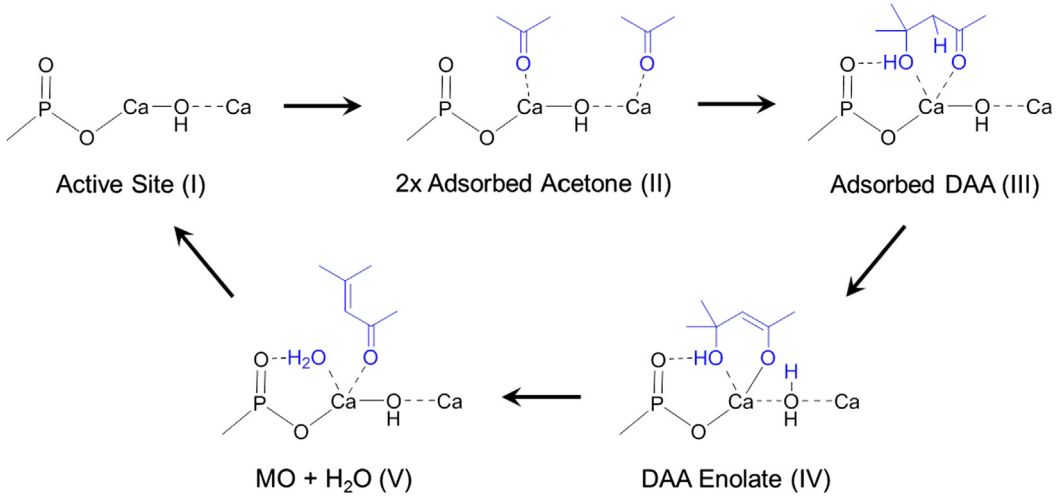

Scheme 2. Mechanism of DAA dehydration over Ca-HAP.

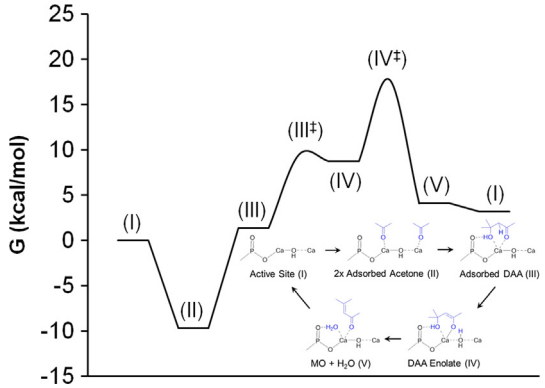

Fig. 7. Free energy profile of acetone condensation over Ca-HAP. Roman numerals refer to the steps shown in the figure and in Scheme 2.

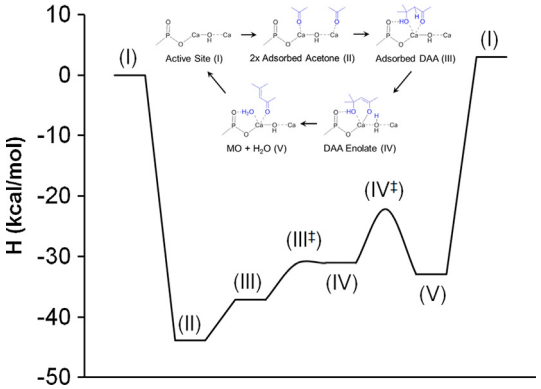

Fig. 8. Enthalpy profile of acetone condensation over Ca-HAP. Roman numerals refer to the steps shown in the figure and in Scheme 2.

adsorption of DAA (**III**), an α-proton is abstracted to form the corresponding enolate (**IV**). Looking at the surface of HAP, the proton can be abstracted either by a surface OH^- group or by a surface PO_4^{3-} group. Enolate formation over an OH group is energetically uphill ($\Delta G_{III\rightarrow IV}$ = +6.4 kcal/mol), with a free energy barrier of +8.1 kcal/mol. The small difference between the thermodynamic and kinetic barriers can be attributed to the mobility of the OH^- group, which can partially rotate around the Ca^{2+} ion to minimize the distance the α-proton has to travel along the reaction coordinate. Enolate formation over a PO_4^{3-} group is more difficult (ΔG = +20.3 kcal/mol) due to the weaker interaction between the α-proton and phosphate group.

Once the enolate is formed, the abstracted α-proton hydrogen bonds with the hydroxyl group on DAA. The hydrogen bond activates the hydroxyl group and stabilizes the transition state during subsequent C—O bond cleavage to form MO (**V**) and an additional OH^- group adsorbed on Ca^{2+}. The activation barrier of this step is $\Delta G^{\ddagger}$ = +9.0 kcal/mol, which is the highest calculated barrier for DAA dehydration, consistent with experimental conclusions that C—O bond cleavage of the enolate is rate-limiting. The previously abstracted α-proton is transferred to the new OH^- group to form water in a barrierless step. Finally, desorption of water and MO complete the catalytic cycle.

To relate the experimental activation energies to DFT calculations, it is necessary to identify the rate-determining intermediate of the system. The experimental activation energies were measured at $P_{acetone}$ = 15 kPa, where the reaction is 0.1 order with respect to acetone (Fig. S7). This indicates that the active sites of HAP are mostly occupied by an adsorbed intermediate. Although the conversion of acetone to MIBK is controlled by the rate of DAA dehydration, it is possible that the most abundant surface intermediate is adsorbed acetone. Acetone adsorbs preferentially onto Ca atoms via its carbonyl oxygen, similar to DAA. To balance the reaction stoichiometry, the adsorption of two acetone molecules was considered. It was found that both acetone molecules could adsorb on the same Ca atom (ΔE = −37.0 kcal/mol) but the most stable geometry involves two acetone molecules adsorbed on adjacent Ca atoms (ΔE = −44.3 kcal/mol, ΔG = −9.7 kcal/mol). This adsorption mode (species **II** in Scheme 2)) was found to be more energetically stable than adsorbed DAA by 11.1 kcal/mol, suggesting that the surface is covered by acetone under reaction conditions. This is what is shown in Fig. 7.

The calculated apparent activation energy for acetone condensation is 21.7 kcal/mol, as seen in Fig. 8, which is higher than the value of 14 kcal/mol measured experimentally. We hypothesize that this difference in activation energies could be attributed to additional bonding interactions between adsorbed intermediates and chemisorbed water formed in situ. Calculations show that the presence of water does not reduce the barrier of enolate formation over HAP. As mentioned previously, the surface hydroxyl group on HAP have a certain degree of mobility around the Ca atom and can orient itself to form a strong bonding interaction with the α-proton of DAA, as demonstrated by the short distance between the α-proton and hydroxyl group in the TS ($H_\alpha—O_{hydroxyl}$ = 1.24 Å, Fig. S8). Thus, a water-mediated proton transfer pathway does not change the activation barrier because the surface hydroxyl group is placed ideally to accept the α-proton. On the other hand, the presence of water plays a beneficial role in stabilizing the leaving hydroxyl group on DAA through multiple hydrogen-bonds during C—O bond cleavage of the enolate (Fig. S9). The electronic barrier decreases from 11.0 kcal/mol to 5.7 kcal/mol, which is similar to the difference between the apparent calculated and experimental activation energies. However, due to the myriad of possible H-bonding configurations over the surface of HAP when water is introduced, it was not feasible to calculate the full reaction pathway accurately in the presence of water.

The electronic energies of the intermediates and barriers for DAA dehydration were also determined for Mg-, Sr- and Ba-exchanged HAP. These materials were modeled by replacing one of the four geometrically equivalent surface Ca atoms in the HAP supercell with another alkaline earth metal, which corresponds to a surface exchange of 25%. The optimized lattice parameters for Mg-, Sr- and Ba-HAP deviated by less than 1% compared to that of the native Ca-HAP, showing that surface cation exchange does not affect the bulk structure.

The electronic adsorption energy of two acetone molecules decreases in the order of Ca-HAP (−45.2 kcal/mol) > Mg-HAP (−44.1 kcal/mol) > Sr-HAP (−42.0 kcal/mol) > Ba-HAP (−38.0 kcal/mol). In all cases, acetone binds in an upright position with the carbonyl oxygen oriented towards a M^{2+} cation. The relative adsorption energies over Ca-, Sr- and Ba-HAP follow the trend that stronger Lewis acids bind acetone more tightly. However, we observed that acetone adsorption on Mg-HAP is weaker than on Ca-HAP, even though Mg^{2+} is a stronger Lewis acid than Ca^{2+}. Closer inspection of the bare surfaces reveals that reorientation of the surrounding phosphate groups allows the smaller Mg^{2+} cation to sit more deeply in the framework than Ca^{2+}, thereby maximizing the bonding interaction with the O atom directly beneath it ($Mg—O_b$ = 2.38 Å, Fig. S10). Local reorientation of surrounding phosphate groups around a smaller cation has also been reported for Ni-, Cu- and Zn-exchanged HAP [55]. Upon adsorption of acetone, the Mg^{2+} cation is displaced upward from the surface enabling it to coordinate with acetone, which causes the Mg—O interaction to weaken ($Mg—O_b$ = 2.65 Å). This phenomena does not occur with the larger Ca^{2+} cation (Fig. S10), which retains a strong coordination to all oxygen atoms in the first shell regardless

of whether the surface is either empty (Ca—O_b = 3.46 Å) or covered in acetone (Ca—O_b = 3.48 Å).

The most stable geometry of adsorbed DAA was found to be identical over all catalysts, with adsorption energies that differed by less than 5 kcal/mol. However, formation of the corresponding enolate was much more favorable over Mg- and Ba-HAP compared to Ca-HAP and Sr-HAP. In the case of Mg-HAP, the smaller Mg^{2+} cation is unable to fully coordinate with every neighboring oxygen atom. Fig. S11 shows that the Mg^{2+} cation adopts a five-coordinate geometry after adsorption of DAA, and forms bonds with one surface hydroxyl oxygen, two phosphate oxygen atoms, and the two oxygen atoms on DAA. After an α-hydrogen atom is abstracted by the surface hydroxyl group to form a surface water species and the corresponding enolate, the stable water molecule can rotate away from Mg^{2+}. This allows Mg^{2+} to shift along the b-axis and coordinate with another phosphate oxygen, resulting in a large energetic stabilization ($\Delta E_{III\rightarrow IV}$ = −4.3 kcal/mol) that is not seen over Ca- or Sr-HAP. A similar stabilization of the enolate is also seen over Ba-HAP, although for different reasons. Because of the large size of Ba^{2+}, the water formed from α-hydrogen abstraction is able to hydrogen bond with two oxygen atoms in the second shell of Ba^{2+} while maintaining coordination with Ba^{2+}, leading to a very stable intermediate ($\Delta E_{III\rightarrow IV}$ = −12.2 kcal/mol). In fact, free energy calculations show that the DAA enolate is more favorable than adsorbed acetone by −14.2 kcal/mol, suggesting that the DAA enolate is the resting state of the catalytic cycle over sites bonded to Ba^{2+}.

As shown in Fig. 9, the set of elementary steps for DAA dehydration was found to be identical over Mg-, Ca- and Sr-HAP. For each catalyst, adsorbed acetone is the resting state. The α-proton of DAA is abstracted, and the subsequent C—O bond cleavage to form adsorbed MO + H_2O is the rate-limiting step. Ba-HAP followed a similar pathway, but the intermediate DAA enolate is more energetically favorable than adsorbed acetone. The calculated electronic barriers for acetone condensation over Mg-, Ca-, Sr- and Ba-HAP are 22.0, 22.1, 20.5 and 21.8 kcal/mol, respectively. The trend in the values of the computed activation energy qualitatively agree with that found experimentally, with Sr-HAP having the lowest activation barrier in both cases. Overall, the calculations reveal that Sr-HAP is the best material because it can catalyze α-proton abstraction and C—O bond cleavage without binding acetone or DAA enolate too strongly. While qualitative descriptors such as Lewis basicity and electronegativity can be used to describe the site requirements for acetone condensation, a deeper understanding of the adsorption geometries is needed to explain why reaction rates over Ba-HAP are lower than the less basic Sr-HAP.

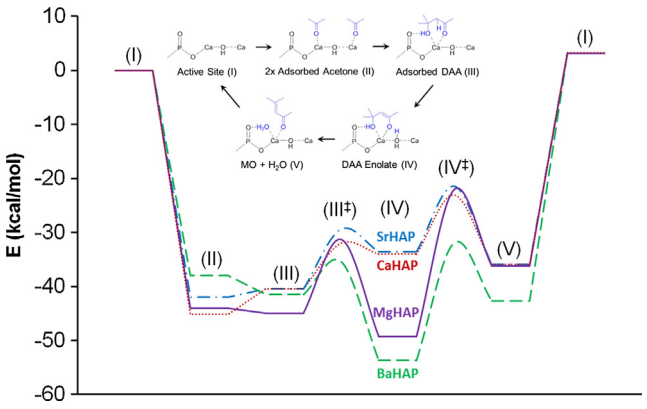

Fig. 9. Electronic energy profile of acetone condensation over Mg-, Ca-, Sr- and Ba-HAP. Roman numerals refer to the steps shown in Scheme 2 and Fig. 7.

The correlations between cation electronegativity and catalytic activity parallel previous findings in literature regarding aldol coupling over alkaline earth metal oxides [64,77,78]. For example, Frey et al. demonstrated that as the electronegativity of the cation decreases (Mg^{2+} → Ba^{2+}), the initial heat of CO_2 adsorption and acetone condensation rate both increase over the corresponding alkaline earth metal oxide [78]. They proposed that strong basic sites enhance the surface enolate concentration which leads to higher reaction rates [62]. Our results show that in the context of aldol dehydration, decreasing cation electronegativity leads to increased reaction rates, with the exception of barium. DFT calculations show that Ba-HAP stabilizes the aldol enolate intermediate more than Mg-, Ca-, or Sr-HAP. This finding is in line with the idea that surfaces with stronger basic sites possess a higher concentration of surface enolate species, consistent with previous literature. Within the HAP framework, a barium substituted version results in overstabilization of the aldol enolate intermediate, leading to lower reaction rates.

4. Conclusions

Acetone condensation to MIBK can be performed in a single step using a physical mixture of HAP and Pd/SiO_2. The initial coupling of acetone to form DAA is equilibrated, and the subsequent dehydration of DAA to form MO is rate-limiting. *In-situ* titrations show that this reaction is base-catalyzed, in line with an E_{1cB} dehydration mechanism. A series of ion-exchanged catalysts were used to investigate the relationship between catalyst acid/base strength and activity. Sr-HAP was found to be the most active catalyst. DFT calculations reveal that the identity of the cation plays an important role in dictating the stability of adsorbed intermediates and the overall reaction barrier. Mg- and Ca-HAP are less active than Sr-HAP because Lewis acidic Mg^{2+} and Ca^{2+} centers bind acetone too strongly. Although Ba^{2+} is less acidic than Sr^{2+}, Ba-HAP is less active than Sr-HAP due to the larger size of Ba^{2+}, which leads to an overstabilization of the enolate intermediate due to additional hydrogen-bonding interactions.

Acknowledgements

This work was funded by Director, Office of Science, Office of Basic Energy Sciences of the U.S. Department of Energy under Contract No. DE-AC02-05CH11231. Calculations were performed on a computing cluster sponsored by the National Institutes of Health (NIH S10OD023532). The authors would like to thank Ezra Clark for help in collecting XPS spectra.

References

[1] S. Sifniades, A.B. Levy, in: Ullmann's Encycl. Ind. Chem., 5th ed., Wiley-VCH, Weinheim, 2005.
[2] K. Weissennel, H. Arpe, Industrial Organic Chemstry, 4th ed., Wiley-VCH, Weinheim, 2003.
[3] W.L. Faith, F.A. Lowenheim, M.K. Moran, Faith, Keyes & Clark's Industrial Chemicals, 4th ed., Wiley, New York, 1975.
[4] S. Shylesh, D. Hanna, J. Gomes, C.G. Canlas, M. Head-Gordon, A.T. Bell, ChemSusChem. 8 (2015) 466–472.
[5] S. Talwalkar, S. Mahajani, Appl. Catal. A Gen. 302 (2006) 140–148.
[6] W. Nicol, E.L. Du Toit, Chem. Eng. Process. Process Intensif. 43 (2004) 1539–1545.
[7] S. Zhang, P. Wu, L. Yang, Y. Zhou, H. Zhong, Catal. Commun. 71 (2015) 61–64.
[8] L.M. Gandía, M. Montes, Appl. Catal. A, Gen. 101 (1993).
[9] P.V.R. Rao, V.P. Kumar, G.S. Rao, K.V.R. Chary, Catal, Sci. Technol. 2 (2012) 1665.
[10] A.A. Nikolopoulos, B.W.-L. Jang, J.J. Spivey, Appl. Catal. A Gen. 296 (2005) 128–136.
[11] Y. Chen, C. Hwang, C. Liaw, Appl. Catal. A Gen. 169 (1998) 207–214.
[12] J.I. Di Cosimo, V.K. Díez, C.R. Apesteguía, Appl. Clay Sci. 13 (1998) 433–449.
[13] S. Shylesh, D. Kim, A.A. Gokhale, C.G. Canlas, J.O. Struppe, C.R. Ho, D. Jadhav, A. Yeh, A.T. Bell, Ind. Eng. Chem. Res. 55 (2016) 10635–10644.
[14] S. Diallo-Garcia, D. Laurencin, J.M. Krafft, S. Casale, M.E. Smith, H. Lauron-Pernot, G. Costentin, J. Phys. Chem. C. 115 (2011) 24317–24327.

[15] K. Elkabouss, M. Kacimi, M. Ziyad, S. Ammar, F. Bozon-Verduraz, J. Catal. 226 (2004) 16–24.
[16] Y. Matsumura, J.B. Moffat, S. Sugiyama, H. Hayashi, N. Shigemoto, K. Saitoh, J. Chem. Soc. Faraday Trans. 90 (1994) 2133.
[17] S. Sugiyama, H. Matsumoto, H. Hayashi, J.B. Moffat, Colloids Surfaces A Physicochem. Eng. Asp. 169 (2000) 17–26.
[18] S. Ogo, A. Onda, K. Yanagisawa, Appl. Catal. A Gen. 348 (2008) 129–134.
[19] Y. Zhu, X. Zhang, F. Long, H. Liu, M. Qian, N. He, Mater. Lett. 63 (2009) 1185–1188.
[20] J.M. Hughes, M. Cameron, K.D. Crowley, Am. Mineral. 74 (1989) 870–876.
[21] C.R. Ho, S. Shylesh, A.T. Bell, ACS Catal. 6 (2016) 939–948.
[22] E.R. Sacia, M. Balakrishnan, M.H. Deaner, K.A. Goulas, F.D. Toste, A.T. Bell, ChemSusChem. 8 (2015) 1726–1736.
[23] S. Ogo, A. Onda, K. Yanagisawa, Appl. Catal. A Gen. 402 (2011) 188–195.
[24] L. Silvester, J.-F. Lamonier, J. Faye, M. Capron, R.-N. Vannier, C. Lamonier, J. Dubois, J. Couturier, C. Calais, F.Y. Dumeignil, Catal. Sci. Technol. 5 (2015) 2994–3006.
[25] L. Silvester, J.-F. Lamonier, C. Lamonier, M. Capron, R.-N. Vannier, A.-S. Mamede, F. Dumeignil, ChemCatChem. 9 (2017) 2250–2261.
[26] L. Silvester, J.F. Lamonier, R.-N.N. Vannier, C. Lamonier, M. Capron, A.S. Mamede, F. Pourpoint, A. Gervasini, F. Dumeignil, J. Mater. Chem. A. 2 (2014) 11073–11090.
[27] A. Yasukawa, T. Yokoyama, K. Kandori, T. Ishikawa, Colloids Surfaces A Physicochem. Eng. Asp. 299 (2007) 203–208.
[28] M. Wakamura, K. Kandori, T. Ishikawa, Colloids Surfaces A Physicochem. Eng. Asp. 142 (1998) 107–116.
[29] A. Yasukawa, T. Yokoyama, K. Kandori, T. Ishikawa, Colloids Surfaces A Physicochem. Eng. Asp. 238 (2004) 133–139.
[30] G. Levinskas, W. Neuman, J. Phys. Chem. 59 (1955) 164–168.
[31] T. Tsuchida, J. Kubo, T. Yoshioka, S. Sakuma, T. Takeguchi, W. Ueda, J. Catal. 259 (2008) 183–189.
[32] S. Hanspal, Z.D. Young, H. Shou, R.J. Davis, ACS Catal. 5 (2015) 1737–1746.
[33] T. Suzuki, T. Hatsushika, Y. Hayakawa, J. Chem. Soc. Faraday Trans. 1 (77) (1981) 1059–1062.
[34] S. Takashi, T. Hatsushika, M. Miyake, J. Chem. Soc., Faraday Trans. 1 (78) (1982) 3605–3611.
[35] J.H. Scofield, Lawrence Livermore Lab. Rep. No. UCRL-51326, 1973.
[36] S. Tanuma, C.J. Powell, D.R. Penn, Surf. Interface Anal. 37 (2005) 1–14.
[37] P. Rulis, L. Ouyang, W.Y. Ching, Phys. Rev. B - Condens. Matter Mater. Phys. 70 (2004) 1–8.
[38] L. Liang, P. Rulis, W.Y. Ching, Acta Biomater. 6 (2010) 3763–3771.
[39] M. Mohai, Surf. Interface Anal. 36 (2004) 828–832.
[40] G. Kresse, J. Furthmüller, Phys. Rev. B. 54 (1996) 11169–11186.
[41] J.P. Perdew, K. Burke, M. Ernzerhof, Phys. Rev. Lett. 77 (1996) 3865–3868.
[42] J.D. Pack, H.J. Monkhorst, Phys. Rev. B. 13 (1976) 5188.
[43] S. Grimme, S. Ehrlich, L. Goerigk, J. Comput. Chem. 32 (2011) 1456–1465.
[44] G. Henkelman, B.P. Uberuaga, H. Jónsson, J. Chem. Phys. 113 (2000) 9901–9904.
[45] G. Henkelman, H. Jónsson, J. Chem. Phys. 111 (1999) 7010–7022.
[46] S. Grimme, Chem. – A Eur. J. 18 (2012) 9955–9964.
[47] Y.P. Li, J. Gomes, S.M. Sharada, A.T. Bell, M. Head-Gordon, J. Phys. Chem. C. 119 (2015) 1840–1850.
[48] M. Corno, C. Busco, B. Civalleri, P. Ugliengo, Phys. Chem. Chem. Phys. 8 (2006) 2464.
[49] C.A. Ospina, J. Terra, A.J. Ramirez, M. Farina, D.E. Ellis, A.M. Rossi, Colloids Surf. B. Biointerfaces. 89 (2012) 15–22.
[50] Y. Shao, Z. Gan, E. Epifanovsky, A.T.B. Gilbert, M. Wormit, J. Kussmann, A.W. Lange, A. Behn, J. Deng, X. Feng, D. Ghosh, M. Goldey, P.R. Horn, L.D. Jacobson, I. Kaliman, R.Z. Khaliullin, T. Kus, A. Landau, J. Liu, E.I. Proynov, Y.M. Rhee, R.M. Richard, M.A. Rohrdanz, R.P. Steele, E.J. Sundstrom, H.L. Woodcock, P.M. Zimmerman, D. Zuev, B. Albrecht, E. Alguire, B. Austin, G.J.O. Beran, Y.A. Bernard, E. Berquist, K. Brandhorst, K.B. Bravaya, S.T. Brown, D. Casanova, C.M. Chang, Y. Chen, S.H. Chien, K.D. Closser, D.L. Crittenden, M. Diedenhofen, R.A. Distasio, H. Do, A.D. Dutoi, R.G. Edgar, S. Fatehi, L. Fusti-Molnar, A. Ghysels, A. Golubeva-Zadorozhnaya, J. Gomes, M.W.D. Hanson-Heine, P.H.P. Harbach, A. W. Hauser, E.G. Hohenstein, Z.C. Holden, T.C. Jagau, H. Ji, B. Kaduk, K. Khistyaev, J. Kim, J. Kim, R.A. King, P. Klunzinger, D. Kosenkov, T. Kowalczyk, C. M. Krauter, K.U. Lao, A.D. Laurent, K.V. Lawler, S.V. Levchenko, C.Y. Lin, F. Liu, E. Livshits, R.C. Lochan, A. Luenser, P. Manohar, S.F. Manzer, S.P. Mao, N. Mardirossian, A.V. Marenich, S.A. Maurer, N.J. Mayhall, E. Neuscamman, C.M. Oana, R. Olivares-Amaya, D.P. Oneill, J.A. Parkhill, T.M. Perrine, R. Peverati, A. Prociuk, D.R. Rehn, E. Rosta, N.J. Russ, S.M. Sharada, S. Sharma, D.W. Small, A. Sodt, T. Stein, D. Stück, Y.C. Su, A.J.W. Thom, T. Tsuchimochi, V. Vanovschi, L. Vogt, O. Vydrov, T. Wang, M.A. Watson, J. Wenzel, A. White, C.F. Williams, J. Yang, S. Yeganeh, S.R. Yost, Z.Q. You, I.Y. Zhang, X. Zhang, Y. Zhao, B.R. Brooks, G.K.L. Chan, D.M. Chipman, C.J. Cramer, W.A. Goddard, M.S. Gordon, W.J. Hehre, A. Klamt, H.F. Schaefer, M.W. Schmidt, C.D. Sherrill, D.G. Truhlar, A. Warshel, X. Xu, A. Aspuru-Guzik, R. Baer, A.T. Bell, N.A. Besley, J. Da Chai, A. Dreuw, B.D. Dunietz, T.R. Furlani, S.R. Gwaltney, C.P. Hsu, Y. Jung, J. Kong, D.S. Lambrecht, W. Liang, C. Ochsenfeld, V.A. Rassolov, L.V. Slipchenko, J.E.Subotnik T. Van Voorhis, J.M. Herbert, A.I. Krylov, P.M.W. Gill, M. Head-Gordon, Mol. Phys. 113 (2015) 184–215.
[51] I. Mobasherpour, M.S. Heshajin, A. Kazemzadeh, M. Zakeri, J. Alloys Compd. 430 (2007) 330–333.
[52] B.O. Fowler, Inorg. Chem. 13 (1974) 194–207.
[53] R. Cuscó, F. Guitián, S. de Aza, L. Artús, J. Eur. Ceram. Soc. 18 (1998) 1301–1305.
[54] A. Hadrich, A. Lautie, T. Mhiri, Spectrochim. Acta – Part A Mol. Biomol. Spectrosc. 57 (2001) 1673–1681.
[55] K. Matsunaga, H. Inamori, H. Murata, Phys. Rev. B – Condens. Matter Mater. Phys. 78 (2008) 1–8.
[56] Y. Matsuura, A. Onda, S. Ogo, K. Yanagisawa, Catal. Today. 226 (2014) 192–197.
[57] Z.D. Young, S. Hanspal, R.J. Davis, ACS Catal. 6 (2016) 3193–3202.
[58] A.M. Hernández-Giménez, J. Ruiz-Martínez, B. Puértolas, J. Pérez-Ramírez, P.C. A. Bruijnincx, B.M. Weckhuysen, Top. Catal. (2017).
[59] K.E. Price, S.J. Broadwater, H.M. Jung, D.T. McQuade, Org. Lett. 7 (2005) 147–150.
[60] L. Do Amaral, H.G. Bull, E.H. Cordes, J. Am. Chem. Soc. 94 (1972) 7579–7580.
[61] H. Zhang, M.Y.S. Ibrahim, D.W. Flaherty, J. Catal. 361 (2018) 290–302.
[62] G. Zhang, H. Hattori, K. Tanabe, Appl. Catal. 40 (1988) 183–190.
[63] F. Winter, a. Jos Van Dillen, K.P. De Jong, J. Mol. Catal. A Chem. 219 (2004) 273–281.
[64] G. Zhang, H. Hattori, K. Tanabe, Appl. Catal. 36 (1988) 189–197.
[65] I.M. Hill, S. Hanspal, Z.D. Young, R.J. Davis, J. Phys. Chem. C. 119 (2015) 9186–9197.
[66] C.L. Kibby, W. Hall, J. Catal. 159 (1973) 144–159.
[67] L.G. Wade, Organic Chemistry, 8th ed., Pearson, Boston, 2012.
[68] C.L. Perrin, K.L. Chang, J. Org. Chem. 81 (2016) 5631–5635.
[69] V.K. Díez, C.R. Apesteguía, J.I. Di Cosimo, Catal. Today. 63 (2000) 53–62.
[70] D.E. Ellis, J. Terra, O. Warschkow, M. Jiang, G.B. González, J.S. Okasinski, M.J. Bedzyk, A.M. Rossi, J.-G. Eon, Phys. Chem. Chem. Phys. 8 (2006) 967–976.
[71] E.G. Rodrigues, T.C. Keller, S. Mitchell, J. Pérez-Ramírez, Green Chem. 16 (2014) 4870–4874.
[72] M. Corno, C. Busco, V. Bolis, S. Tosoni, P. Ugliengo, Langmuir 25 (2009) 2188–2198.
[73] F. Peccati, C. Bernocco, P. Ugliengo, M. Corno, J. Phys. Chem. C. 122 (2018) 3934–3944.
[74] S. Diallo-Garcia, M.B. Osman, J.M. Krafft, S. Boujday, C. Guylène, Catal. Today 226 (2014) 81–88.
[75] M. Ben Osman, S. Diallo Garcia, J.-M. Krafft, C. Methivier, J. Blanchard, T. Yoshioka, J. Kubo, G. Costentin, Phys. Chem. Chem. Phys. 18 (2016) 27837–27847.
[76] J.A.S. Bett, L.G. Christner, W. Keith Hall, J. Am. Chem. Soc. 89 (1967) 5535–5541.
[77] A. Corma, S. Iborra, Optimization of Alkaline Earth Metal Oxide and Hydroxide Catalysts for Base-Catalyzed Reactions, Elsevier Masson SAS, 2006.
[78] A.M. Frey, J. Yang, C. Feche, N. Essayem, D.R. Stellwagen, F. Figueras, K.P. De Jong, J.H. Bitter, J. Catal. 305 (2013) 1–6.